Geophysical Research Letters

RESEARCH LETTER
10.1029/2019GL084117

Eddy Saturation of the Southern Ocean: A Baroclinic Versus Barotropic Perspective

Navid C. Constantinou[1] **and Andrew McC. Hogg**[1]

[1]Research School of Earth Sciences and ARC Centre of Excellence for Climate Extremes, Australian National University, Canberra, ACT, Australia

Key Points:
- An isopycnal layered model is used to assess the relative importance of barotropic and baroclinic processes in the Southern Ocean
- Both baroclinic and barotropic flows exhibit regimes in which the mean zonal transport is insensitive to wind stress
- Eddies actively shape the time-mean flow, irrespective of the instabilities from which they originate

Correspondence to:
N. C. Constantinou,
Navid.Constantinou@anu.edu.au

Citation:
Constantinou, N. C., & Hogg, A. M. (2019). Eddy saturation of the Southern Ocean: A baroclinic versus barotropic perspective. *Geophysical Research Letters*, *46*, 12,202–12,212. https://doi.org/10.1029/2019GL084117

Received 14 JUN 2019
Accepted 10 SEP 2019
Accepted article online 13 SEP 2019
Published online 9 NOV 2019

Abstract "Eddy saturation" is the regime in which the total time-mean volume transport of an oceanic current is relatively insensitive to the wind stress forcing and is often invoked as a dynamical description of Southern Ocean circulation. We revisit the problem of eddy saturation using a primitive equations model in an idealized channel setup with bathymetry. We apply only mechanical wind stress forcing; there is no diapycnal mixing or surface buoyancy forcing. Our main aim is to assess the relative importance of two mechanisms for producing eddy-saturated states: (i) the commonly invoked baroclinic mechanism that involves the competition of sloping isopycnals and restratification by production of baroclinic eddies and (ii) the barotropic mechanism that involves production of eddies through lateral shear instabilities or through the interaction of the barotropic current with bathymetric features. Our results suggest that the barotropic flow component plays a crucial role in determining the total volume transport.

Plain Language Summary Wind stress at the surface of the ocean is an important driver of ocean currents. However, what sets up the strength of the currents remains puzzling. The strongest ocean current flows around Antarctica: the Antarctic Circumpolar Current. It is believed that the Antarctic Circumpolar Current is close to a so-called "eddy-saturated" state, a regime in which changes in the strength of the wind stress forcing do not alter the strength of the mean current. Instead, the swirling oceanic eddy motions that accompany the current are enhanced. Here, we investigate the physics and assess the relative importance of the two mechanisms proposed in the literature to explain this phenomenon: the most commonly invoked baroclinic mechanism and the recently proposed barotropic mechanism that crucially involves the interaction of the oceanic flow with bathymetric features. Our results suggest that the oftentimes ignored depth-averaged (barotropic) component of the ocean flow and its interaction with bathymetry play a dominant role in setting up the strength of the current in certain regimes.

1. Introduction

The Southern Ocean, and in particular the Antarctic Circumpolar Current (ACC) that connects all ocean basins, influences the global ocean circulation and the climate (Ferrari et al., 2014; Talley, 2013; Toggweiler et al., 2006). The circulation in the Southern Ocean is fueled by a combination of the strong westerly winds imparting momentum at the ocean's surface and by surface buoyancy forcing. In the last few decades the strength of the westerly winds over the Southern Ocean is increasing as a response to climate change forcing and ozone depletion (Farneti et al., 2015; Marshall, 2003; Swart & Fyfe, 2012; Bracegirdle et al., 2013). Thus, significant effort has been expended to understand how the ACC will respond to this wind increase. However, several questions remain outstanding.

One idea that has emerged is that the ocean is in a so-called "eddy-saturated" state, in which stronger winds do not increase the mean strength of the current. Instead, the additional work done by wind increases the energy of the mesoscale eddies. This idea was first hypothesized by Straub (1993); since then a series of eddy-resolving ocean models, both idealized and more realistic, have verified that the ACC is close to the so-called eddy-saturated limit (e.g., Abernathey & Cessi, 2014; Dufour et al., 2012; Farneti et al., 2010; Hallberg & Gnanadesikan, 2001, 2006; Hogg et al., 2008; Marshall et al., 2017; Meredith et al., 2012; Munday et al., 2013; Tansley & Marshall, 2001). The eddy saturation hypothesis is not contradicted by observations (Böning et al., 2008; Firing et al., 2011; Hogg et al., 2015).

In a seminal paper Munk and Palmén (1951) argued that zonal momentum in the Southern Ocean is balanced primarily through "topographic form stress," rather than by bottom drag. Topographic form stress is an inviscid mechanism that couples the ocean to the solid Earth through correlations between the bathymetric slopes and the bottom pressure. Since the work by Munk and Palmén (1951) it has been recognized that bathymetry and topographic form stress play a key role in setting the ACC transport.

Similar to topographic form stress, "interfacial form stress" describes the coupling between layers of different densities and is responsible for the vertical transfer of momentum between those layers (Johnson & Bryden, 1989; Olbers et al., 2004; Ward & Hogg, 2011). In this sense, interfacial form stress requires variation of density in the vertical. The usual notion, which goes back to Johnson and Bryden (1989), is that at equilibrium interfacial form stress transfers eastward momentum downward from the surface to the bottom of the ocean, where topographic form stress acts to transfer this momentum to the solid Earth. Ward and Hogg (2011) demonstrated that when the wind stress at the ocean surface changes, rapid barotropic signals form (within several days). Such a fast barotropic response to changes in the wind can be seen in the Southern Ocean State Estimate (Masich et al., 2015), and it is expected; the wind stress projects directly onto the barotropic mode. Moreover, this response induces topographic form stress that balances a large fraction of the imparted momentum from the surface directly to the bottom. Therefore, a corollary stemming from the work by Ward and Hogg (2011) is that the equilibrium of the sort envisaged by Johnson and Bryden (1989) is established when downward transfer of eastward momentum from the surface balances upward transfer of westward momentum from the bathymetry.

The most common explanation for how eddy-saturated states are established relies on the generation of eddies through baroclinic instability (see, e.g., Marshall et al., 2017; Nadeau & Straub, 2012; Straub, 1993). The role of bathymetry in setting up the ACC transport is acknowledged in this explanation, although the role of bathymetry in eddy generation is unclear. However, isolated bathymetric features can have a large effect on the transient (time-dependent) eddy field through localized baroclinic instability and also by producing an associated almost-barotropic standing (time-mean) eddy field pattern (Abernathey & Cessi, 2014).

The baroclinic view of eddy saturation is consistent with the notion that ACC transport is dominated by the "thermal wind transport"—the transport that is diagnosed from the density field alone, that is, by integrating the thermal wind balance twice assuming zero velocity at the bottom of the ocean. Thus, thermal wind transport can be easily inferred from hydrography measurements of the density. Furthermore, the thermal wind transport is related to baroclinic instability, since the vertical shear fuels production of eddies through baroclinic instability. Therefore, considerable effort has been put in explaining why the "thermal wind" transport of the ACC is saturated (see, e.g., Marshall et al., 2017).

However, the notion of zero mean flow at the bottom of the ocean (as the thermal wind transport assumes) has been, recently, challenged. Donohue et al. (2016) made detailed measurements at the ocean floor of Drake Passage (cDrake experiment) and found time-mean bottom flows as strong as about 0.1 m/s. (Time-mean here is understood as the average over the 4 years that the cDrake experiment was in operation.) Thus, the bottom flow can substantially contribute to the total transport. Characteristically, the findings of Donohue et al. (2016) resulted in the "nominal" value of the Drake Passage transport increasing from around 130 to about 170 Sv (Sv = 10^6 m^3/s). Similar findings regarding the importance of bottom flows in the Southern Ocean were also made from satellite altimetry and output from the Southern Ocean State Estimate (Masich et al., 2015; Peña Molino et al., 2014; Rintoul et al., 2014). These findings argue that, although the focus has been for long centered around the thermal wind transport, the barotropic component of the flow may play an important role in setting up the ACC transport.

In addition to the evidence for strong bottom flows, some recent work has emphasized the importance of the bathymetry in setting up standing meanders in the course of the ACC and in producing strong interaction between barotropic and baroclinic fluid motions (Barthel et al., 2017; Youngs et al., 2017). Furthermore, these meanders play a crucial role in balancing the momentum through topographic form stress and thus determining the ACC transport (Katsumata, 2017; Thompson & Naveira Garabato, 2014). These papers further argue for the importance of the barotropic mode in setting up the strength of the transport. Recent work has highlighted that eddy-saturated states can be obtained even without any baroclinicity, that is, in a barotropic ocean of constant density (Constantinou, 2018; Constantinou & Young, 2017). For the establishment of this "barotropic eddy saturation" the bathymetry plays a crucial role. Without any baroclinicity

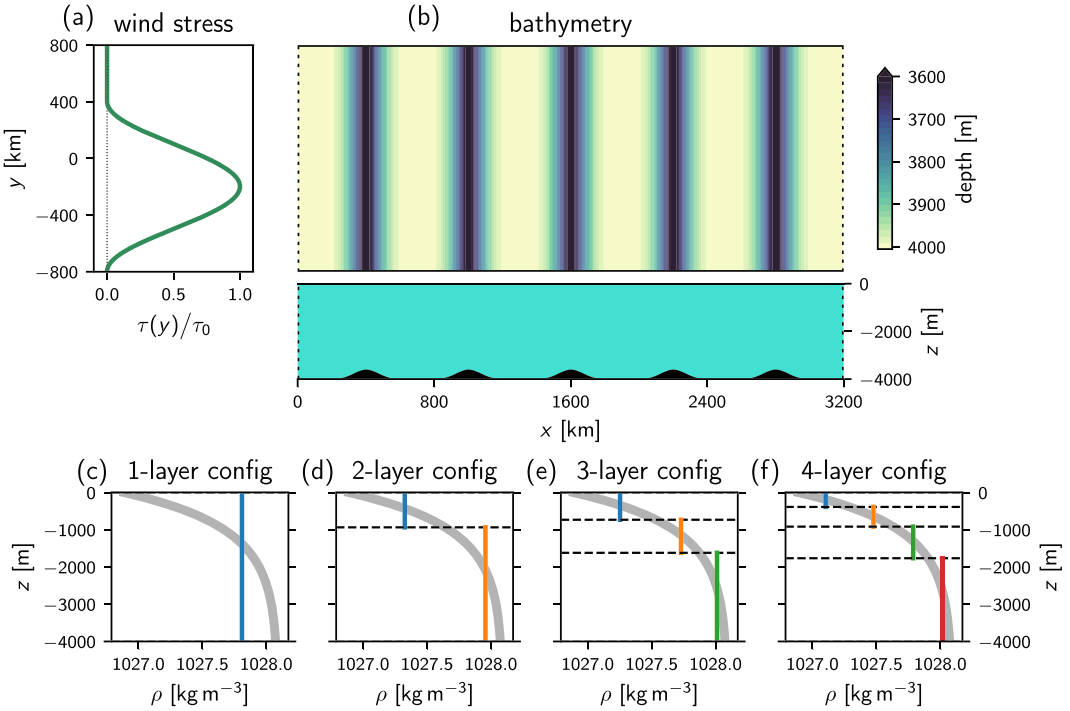

Figure 1. (a) The meridional structure of the imposed wind stress. (b) The bathymetry; top (x-y) and side (x-z) view. (c–f) The layered discretizations of the reference density $\rho(z)$ (shown in solid gray). Dashed horizontal lines depict the rest heights of the various fluid layers, while vertical solid lines denote the mean density of the corresponding fluid layer.

the ocean must rely on instabilities due to lateral shear of the flow or due to the interaction of the flow with bathymetric features (Charney & Flierl, 1980; Hart, 1979).

In this work, we examine the relative importance of the barotropic and baroclinic processes in establishing an eddy-saturated transport. We use a primitive equations model in an idealized zonally reentrant channel that is forced solely by wind stress. There is no diapycnal mixing or surface buoyancy forcing. With this setup we depart from the quasi-geostrophic approach taken by Constantinou (2018), while our model remains computationally tractable to enable us to span a wide range in parameter space. An important advantage of using an isopycnal layered model is that we can vary the stratification in a self-consistent manner that allows us to identify the contributions of baroclinicity in setting up the mean transport.

2. Setup

We use the Modular Ocean Model version 6 (Adcroft et al., 2019) to solve the primitive equations in isopycnal coordinates under the Boussinesq approximation and with a free surface. The model is set up in a zonally reentrant channel on a beta plane. The channel is 3,200 km long in the zonal direction, 1,600 km wide in the meridional direction, 4 km deep, and contains several Gaussian ridges with maximum height of 400 m and full width at half maximum of 165 km; see Figure 1b for details. The horizontal grid cells are squares with 4-km grid spacing. The Coriolis parameter is $f = f_0 + \beta y$ with $f_0 = -10^{-4}$ s and $\beta = 1.5 \times 10^{-11}$ 1/(m s); these values are typical of the Southern Ocean. We include frictional quadratic bottom drag with coefficient 0.003, biharmonic lateral viscosity with coefficient 1.5×10^9 m^4/s, and free-slip insulating sidewalls. We force the model with an imposed steady eastward wind stress that is zonally symmetric and has a meridional structure

$$\tau(y) = \tau_0 \sin^2\left[\frac{\pi(y + L_y/2)}{3L_y/4}\right], \quad \text{for} \quad -\frac{L_y}{2} \le y \le \frac{L_y}{4}, \tag{1}$$

shown in Figure 1a.

A nominal value for wind stress magnitude over the Southern Ocean is about 0.15 N/m^2 (Risien & Chelton, 2008). Given the idealization of the wind stress (1) (steady forcing; no time variability) and also the difference

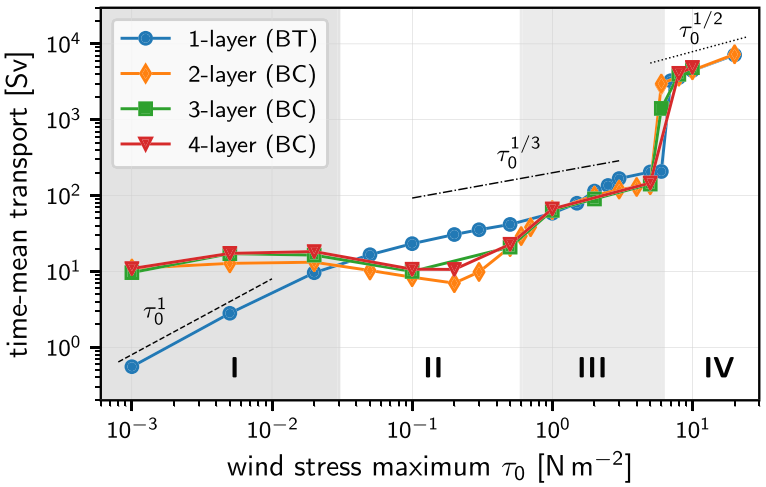

Figure 2. The time-mean transport as a function of the wind stress forcing for the various barotropic (BT) and baroclinic (BC) configurations. Shadings mark the flow regimes discussed in section 3.1. (Sv = 10^6 m^3/s).

in the latitudinal extent of the forcing, we span 4 orders of magnitude in our experiments: 10^{-3} N/m^2 $\lessapprox \tau_0 \lessapprox$ 10 N/m^2. This approach ensures that we cover realistic parameter regimes while also pushing the system to its limits.

The density profile is assumed to follow an exponential form,

$$\rho(z) = \rho_0 + \Delta\rho(1 - e^{z/d}), -H \leq z \leq 0, \tag{2}$$

with $\rho_0 = 1026.89$ kg/m^3, $\Delta\rho = 1.20$ kg/m^3, and $d = 950$ m. Using a least squares fit, we discretize this continuous density profile into n fluid layers, where $n = 1, 2, 3, 4$ (Figures 1c–1f). The discretization is designed to minimize variation in the first Rossby radius of deformation with the number of layers. In each case the first Rossby radius is 20 ± 1 km; the continuous density profile $\rho(z)$ implies a deformation radius of 19.3 km (LaCasce, 2012). These values of Rossby radius lie within the range found across the Southern Ocean (Chelton et al., 1998).

This self-consistent manner of increasing fluid layers to approach the continuous density structure, $\rho(z)$, allows us to isolate the barotropic dynamics when $n = 1$ from the combined effect of barotropic and baroclinic dynamics when $n \geq 2$. We then investigate the effects of these dynamics on the structure of the flow and on the response of the mean current to wind stress forcing. In the following sections, we refer to the density discretization as "n layer configuration." On the other hand, flow in the middle layer of the three-layer configuration is referred to as "the layer two flow'.

3. Results

All simulations presented are well equilibrated; the time series of kinetic energy in each layer and potential energy for each interface reached statistical stationarity. The equilibration times differ from case to case. For example, barotropic single-layer runs reach statistical equilibrium about 5 years after starting from rest, while weakly forced ($\tau_0 < 0.01$ N/m^2) baroclinic runs need up to 500 years to spin up. After the flow equilibrates, we average (for at least 30 years) to obtain the time-mean fields.

3.1. Total Time-Mean Transport

Figure 2 shows the equilibrated time-mean zonal transport of the channel as a function of the wind stress maximum (τ_0) for each configuration. The total transport is computed as the time-mean of $\sum_k \int_0^{L_y} u_k h_k \, \mathrm{d}y$ evaluated at a fixed x, where u is the zonal flow, h is the layer depth, and subscript k denotes each fluid layer with $k = 1$ corresponding to the top layer. For a detailed exposition of the primitive equations in isopycnal coordinates the reader is referred to the paper by Ward and Hogg (2011).

The results from the barotropic runs (single-layer configuration) are qualitatively similar to those of Constantinou and Young (2017) and Constantinou (2018). For very weak wind stress forcing ($\tau \leq$ 0.02 N/m^2) the transport increases linearly with wind stress. For intermediate values of wind stress forcing

($0.05\ \mathrm{N/m^2} \leq \tau_0 \leq 6.0\mathrm{N/m^2}$) the flow develops transient eddies and the transport becomes less sensitive to wind stress forcing. Here, during a 120-fold increase in wind stress the time-mean transport only increases 12-fold (from 17 to 211 Sv). Lastly, for higher values of the wind stress forcing ($\tau \geq 7.0\ \mathrm{N/m^2}$) the flow abruptly transitions to a new regime with higher transport, in which the transport scales as $\tau_0^{1/2}$ (shown in Figure 2).

The baroclinic configurations ($n \geq 2$) show similar behavior among themselves and, in part, different behaviors compared with the single-layer barotropic runs. For wind stress forcing values $\tau_0 \leq 0.5\ \mathrm{N/m^2}$ the time-mean transport remains practically insensitive to wind stress forcing; we even see a decrease of the transport with wind stress forcing (discussed further in section 3.3). For $\tau_0 \geq 1.0\ \mathrm{N/m^2}$, the transport from the baroclinic configurations coincides with those from the single-layer barotropic runs and follows the same transition to the bottom drag-dominated, so-called, "upper-branch" regime.

In summary, Figure 2 suggests that there exist four different regimes (marked I through IV):

I. The baroclinic cases show weak sensitivity on the total transport with wind stress; for barotropic runs the transport is lower than the corresponding baroclinic cases and grows linearly with wind stress.
II. The transport for barotropic cases exceeds that of baroclinic cases. The transport for barotropic runs grows at a rate much less than linear with wind stress; the transport for baroclinic runs decreases slightly.
III. The baroclinic and barotropic cases show almost identical transports; these transports continue to grow at a rate much less than linear with wind stress.
IV. The total transport both for barotropic and baroclinic cases undergoes an abrupt transition to much higher values (the upper branch).

Note that Figure 2 only presents time-mean values. Although transport values for barotropic and baroclinic configurations are similar in certain flow regimes, the baroclinic flows are much more time varying; more details on this in section 3.4.

Since all baroclinic runs show qualitatively similar behavior we will, from hereafter, concentrate only on the purely barotropic one-layer configuration and the baroclinic two-layer configuration.

3.2. Flow Structure Comparison

It is instructive to compare snapshots of statistically equilibrated flow for selected cases. Figure 3 shows flow speed for different values of wind stress, one for each of the four different regimes described above. The left column of Figure 3 shows snapshots from barotropic one-layer configuration, while the middle and right columns show snapshots from baroclinic two-layer configurations. Middle column shows top layer speed, $|u_1|$, and right column shows the depth-averaged flow speed, $\sum_k h_k|\boldsymbol{u}_k|/h$, where $h = \sum_k h_k$ is the total depth. Note how different the flow structure is between the barotropic and baroclinic configurations, even for wind stress forcing $\tau_0 \geq 1.0\ \mathrm{N/m^2}$ for which the total transport is identical among all layered configurations.

For weakly forced cases (the flow Regime I; Figures 3a–3c) the barotropic flow is steady with no eddies and follows the geostrophic contours, f/h. On the other hand, the baroclinic flow of Figure 3b and 3c shows multiple jets and eddies that resemble homogeneous baroclinic turbulence; the top layer flow shows only a weak imprint of the bathymetry. In the flow Regime II (Figures 3d–3f) the barotropic flow starts developing transient eddies but is steered by the bathymetry, while the baroclinic flow shows an imprint of the bathymetry itself. For wind stress values within the flow Regime III (Figures 3g–3i) both barotropic and baroclinic flows show a strong imprint of the bathymetry while the baroclinic flow continues to be much more eddying. Finally, at the upper-branch flow Regime IV (Figures 3j–3l) the barotropic runs develop a strong jet spanning all latitudes where wind stress is nonzero. The top layer baroclinic flow is very different in this case: it outcrops at the surface (see Figure 3k) and is dominated by inertial eddies. These snapshots highlight the great differences in flow regimes that occur, despite the relative insensitivity of the time-mean zonal transport among the various layered configurations in flow Regimes III and IV. A plausible rationalization for why higher wind stress values lead to similar time-mean transport for the various layered configurations is that more eddies imply more vertical momentum transfer through interfacial form stress leading to barotropization of the flow.

The following subsections describe the different processes that are involved in determining the flow structure and the time-mean total transport (Figures 2 and 3).

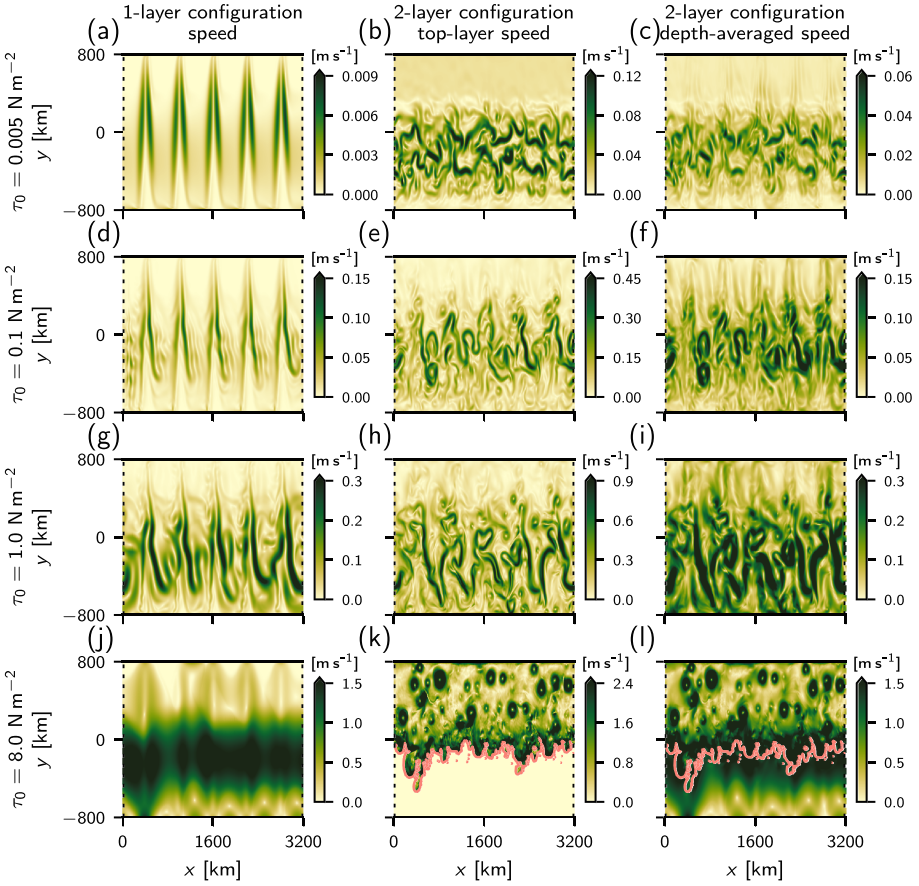

Figure 3. Snapshots of the flow speed for one-layer and two-layer configurations and various wind stress forcing values. (a, d, g, j) and (b, e, h, k) Snapshots of the top layer flow speed. (c, f, i, l) Depth-averaged flow speed for the two-layer configuration. In all baroclinic configurations ($n \geq 2$) the top fluid layer outcrops when the flow is on the upper branch. The pink contours in panels (k) and (l) show the contour $h_1 = 0$, that is, where the top layer outcrops. Despite the dramatic difference in flow structure, the time-mean transport is the same between the one-layer and two-layer configurations for cases with $\tau_0 = 1.0$ N/m^2 and $\tau_0 = 8.0$ N/m^2, respectively.

3.3. Transport per Fluid Layer and Momentum Balance

First, let us see how the total time-mean transport for the baroclinic two-layer runs in Figure 2 is split across fluid layers. Figures 4a and 4b show the decomposition of the time-mean transport into each fluid layer. What we immediately notice in Figure 4b is that for $\tau_0 \leq 0.5$ N/m^2 the bottom layer has a westward (negative) time-mean transport. (We find such bottom layer westward flows in all baroclinic runs for $n = 2, 3, 4$ fluid layers; not shown.)

The depth-integrated zonal momentum balance implies that the wind stress (WS) at the surface must be balanced by a combination of topographic form stress (TFS) and bottom drag (BD) in the bottom layer:

$$\underbrace{\langle \tau \rangle}_{\text{WS}} = \underbrace{\left\langle \overline{p_{\text{bot}}\, \partial_x h_{\text{bot}}} \right\rangle}_{\text{TFS}} + \underbrace{\left\langle \rho_{\text{m}} c_D \overline{|\boldsymbol{u}_n| u_n} \right\rangle}_{\text{BD}}, \tag{3}$$

where angle brackets denote layer average and overbars denote time average, h_{bot} is the bathymetry, and p_{bot} is the bottom pressure.

Figures 4c and 4d show how the topographic form stress and bottom drag on the right-hand side of ((3)) contribute to balance the wind stress on the left-hand side. What stands out is that for most of the wind stress values, the main momentum balance is between wind stress and topographic form stress. Only in the upper-branch flow Regime IV does this momentum balance change. The flow in the upper branch barely feels the bathymetry, the topographic form stress becomes negligible, and bottom drag balances the wind stress resulting in very large time-mean transports. If the wind stress is to be balanced solely by the bottom

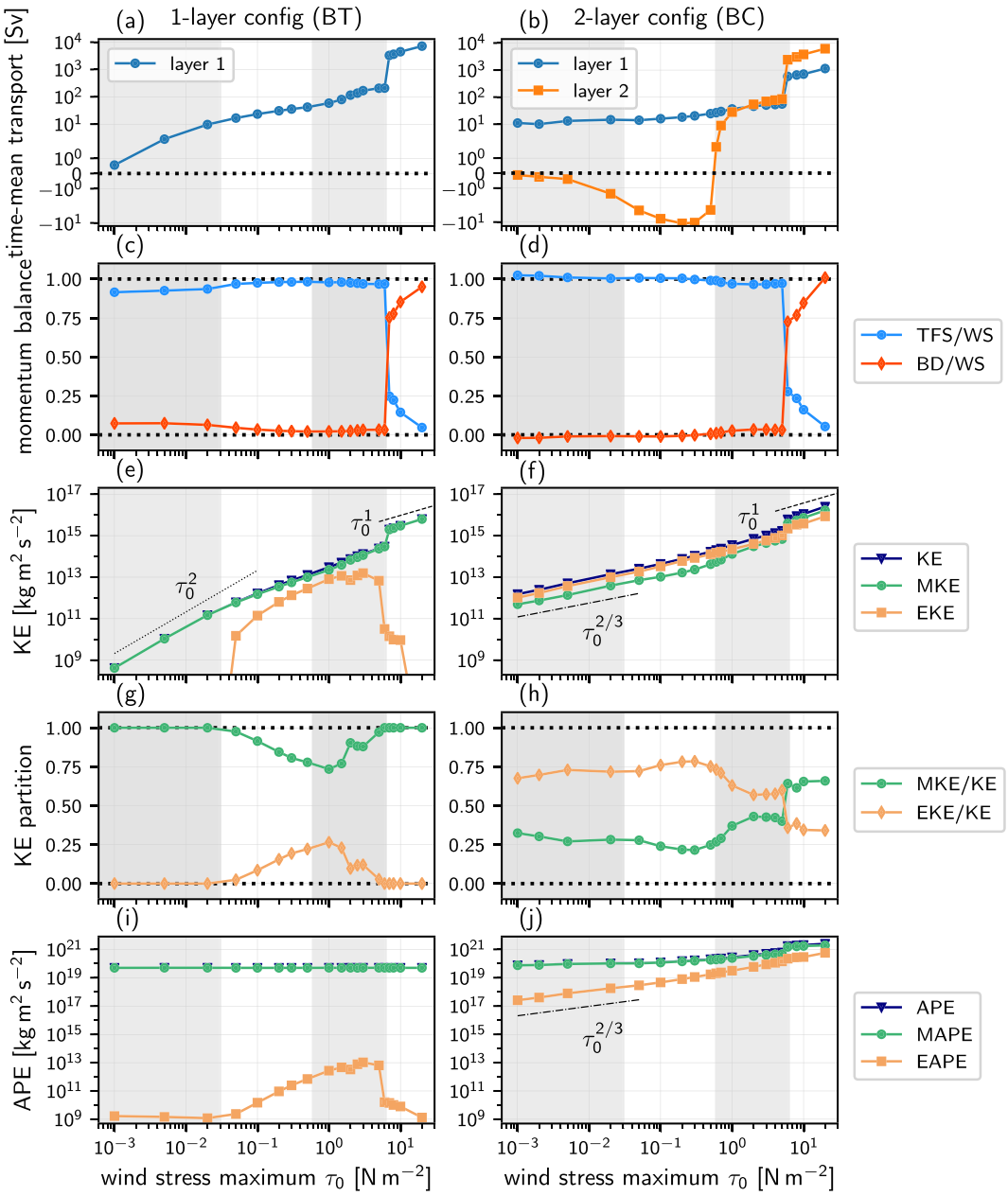

Figure 4. (a, b) The contribution to the time-mean transport from each fluid layer for the one-layer and two-layer configurations shown in Figure 2. (c, d) The ratio of the integrated zonal momentum balanced by topographic form stress over the momentum imparted by wind stress, TFS/WS, and, similarly, the momentum balanced by bottom drag, BD/WS. Note that in panel (d) the bottom drag balance is actually slightly negative for $\tau_0 \leq 0.5\text{N/m}^2$ as a result of the westward bottom layer transport. (e, f) The total kinetic energy (KE), the mean kinetic energy (MKE), and the eddy kinetic energy (EKE). (g, h) The ratios MKE/KE and EKE/KE. (i, j) The total available potential energy (APE), the mean available potential energy (MAPE), and the eddy available potential energy (EAPE). In all panels background shading separates the various flow regimes I–IV described in Figure 2.

drag, then $\tau_0 \propto |u_n|u_n$ implying that transport should scale with $\tau_0^{1/2}$ as seen in Figure 2. Note that both the upper branch flow Regime IV and the far left part of flow Regime I are not expected to be realized in the Southern Ocean, as they occur for unrealistically strong or weak values of the wind stress, respectively. The transition to the upper branch is precisely what was found previously in quasi-geostrophic single-layer simulations (Constantinou, 2018; Constantinou & Young, 2017). In the simpler quasi-geostrophic setup this transition to the upper branch is expected. One may obtain a lower bound for the volume-averaged zonal

velocity, and by imposing the extra restriction that the potential enstrophy power integral is balanced, one finds that the value of this lower bound increases with wind stress. Thus, for high enough wind stress values a transition to the upper branch must occur (Constantinou & Young, 2017). The same transition occurs here in baroclinic runs. Regardless of whether the flow configuration is barotropic or baroclinic, the depth-averaged flow must obey this lower bound.

The depth-integrated momentum balance (3) helps us elucidate the bottom layer westward flows in baroclinic configurations. With a flat bottom, topographic form stress vanishes and thus the bottom layer zonal flow has to be, on average, eastward. Thus, westward flows only appear with nontrivial bathymetry. Provided that topographic form stress is on average positive and balances most of the wind stress, the zonal flow can have either sign (since the sign of the zonal flow does not affect the topographic form stress). The topographic form stress is determined by the time-mean bottom pressure (which is in turn determined by the time-mean position of all fluid interfaces above), and the mean bottom pressure can be configured so that topographic form stress is positive even if zonal flow is negative. (Note that similar westward bottom zonal flows were reported also, e.g., by Treguier & McWilliams (1990) and Stevens & Ivchenko (1997). There is also some observational evidence of such bottom westward flows in certain regions of the Southern Ocean Cunningham and Barker (1996). These westward flows are responsible for the slight decrease in total transport with increasing wind stress that is observed in baroclinic configurations in flow Regime II of Figure 2. However, because of the strong sensitivity to bathymetry, we conclude that the development of bottom westward flow is not a robust feature of this stress-driven configuration. For example, a single ridge of the same height does not result in any bottom layer westward flow (not shown here) and, therefore, the transport in that case does not show any decrease for baroclinic configurations in Regime II.

3.4. Time-Mean-Transient Kinetic Energy

The differences of the barotropic and the baroclinic runs are more pronounced when we inspect the time-mean-transient energy decomposition of the kinetic energy (KE). Consider the standing-transient flow decomposition, $\boldsymbol{u} = \bar{\boldsymbol{u}} + \boldsymbol{u}'$, where prime denotes fluctuations about the time average. Figures 4e–4h depict the integrated mean kinetic energy (MKE), $\sum_k \int \frac{1}{2}\rho_m |\bar{\boldsymbol{u}}_k|^2 \mathrm{d}x\mathrm{d}y$, and the eddy kinetic energy, $\sum_k \int \frac{1}{2}\rho_m \overline{|\boldsymbol{u}'_k|^2}\mathrm{d}x\mathrm{d}y$, with ρ_m the mean reference density. What stands out is that for the barotropic cases, the MKE dominates over the eddy kinetic energy, while for baroclinic cases the opposite is true. For barotropic cases the eddies are negligible for wind stress values within flow Regime I (in which we have linear scaling for total transport) and within flow Regime IV (upper branch). Figures 4i and 4j show the integrated mean available potential energy, $\sum_k \int \frac{1}{2}\rho_m g'_{k-0.5}\overline{\eta_{k-0.5}}^2 \mathrm{d}x\mathrm{d}y$, and the eddy available potential energy, $\sum_k \int \frac{1}{2}\rho_m g'_{k-0.5}\overline{\eta'^2_{k-0.5}}\mathrm{d}x\mathrm{d}y$, where $\eta_{k-0.5}$ is the deviation from rest of the fluid interface between layers k and $k-1$ and $g'_{k-0.5}$ is the corresponding reduced gravity of that interface. The available potential energy is, in general, much larger than the corresponding kinetic energy. Furthermore, in both barotropic and baroclinic runs mean available potential energy dominates over the eddy available potential energy.

As we expect, the baroclinic cases have a more vigorous eddy field, since baroclinic instability is very effective in diverting available potential energy to transient kinetic energy. Even for the weakly forced baroclinic cases in Regime I, after long enough spin up, the top layer fluid is accelerated to the point that the vertical shear is sufficiently large to render the flow baroclinically unstable. In contrast, Figure 4e shows that the barotropic runs with weak wind stress are steady without transients. However, even for these weakly forced baroclinic cases, at equilibrium a time-mean flow must develop if topographic form stress is to balance most of the wind stress. It is interesting that the time-mean flow still accounts for about 25% of the total kinetic energy (see Figure 3h). One might expect that the 25% ratio is determined by the height of bathymetry. However, varying the height of the bathymetric features, we found (not shown) that the ratio MKE/KE remains roughly constant until the bathymetry is small enough so that the topographic form stress fails to balance the wind stress and bottom drag takes over in (3). For our channel, this transition occurs when bathymetric features are less than about 100 m tall (not shown).

4. Discussion and Conclusions

We outlined here a hierarchy of idealized models which have been used to investigate the relative contribution of baroclinic and barotropic processes in establishing zonal transport in a Southern Ocean-like channel. The models presented here are idealized in many respects (the geometry used, the simple bathymetry, constant wind stress, and the lack of diapycnal mixing or surface buoyancy forcing). Furthermore, the

bathymetry we used does include any blocked geostrophic contours, f/h. Using bathymetry with blocked f/h contours results in much less transient eddy activity for the one-layer flow configurations. In addition, as Masich et al. (2015) found, most topographic form stress in the Southern Ocean occurs when the flow meets continents, while our setup is restricted to relatively small ridges. Regardless of these idealizations, these models capture the basic processes involving the wind-driven component of the ACC.

A key outcome is that there exist parameter ranges (flow Regimes II and III) in which both barotropic and baroclinic configurations show similar time-mean zonal transport values and also weak sensitivity of the transport values to wind stress (Figure 2). This similarity in transport occurs despite dramatic differences in eddying flow (as can be seen, e.g., in Figures 3 and 4e–4h). Our analysis shows that within flow Regimes II and III the presence of transient eddies, regardless whether these eddies originate from baroclinic instability or other instabilities, renders the time-mean transport insensitive to wind stress forcing.

The similarity we find between the transport of the barotropic and the baroclinic configurations does not imply that the Southern Ocean is barotropic. Stratification and baroclinic mesoscale eddies are an integral element of the Southern Ocean; mesoscale eddies play a key role in overturning circulation, vertical heat transport, and isopycnal tracer transport. However, the agreement in the values of the time-mean transport among flows with different layer configurations despite differences in the eddy flow supports the notion that bathymetry actively shapes the standing eddy flow which in turn limits the transport through the topographic form stress.

The notion that a regime resembling eddy saturation can be found in a barotropic fluid challenges the widely held view that eddy saturation is a consequence of baroclinic instability acting to optimize isopycnal slopes (Marshall et al., 2017; Straub, 1993). The time-mean depth-integrated momentum balance (equation (3)) implies that the mean topographic form stress is generated purely from the interaction between bathymetric slopes and the time-mean flow. This is easily seen by decomposing the bottom pressure into its standing and transient components,

$$\mathrm{TFS} = \left\langle \overline{p_{\mathrm{bot}}\,\partial_x h_{\mathrm{bot}}} \right\rangle = \left\langle \overline{p_{\mathrm{bot}}}\,\partial_x h_{\mathrm{bot}} \right\rangle . \tag{4}$$

Thus, transient eddies can affect the net momentum balance only if they influence time-mean flow. For symmetric bathymetric features, like the Gaussian ridges we used here, a pressure field which is symmetric upstream and downstream a ridge does not result in mean topographic form stress. Friction alone is able to produce asymmetric flows over symmetric ridges, and therefore topographic form stress, even without transients. However, from the line of reasoning above, we infer that transient eddies (generated either by baroclinic instability or barotropic processes) act to sharpen and barotropize flow over bathymetry, leading to an even more asymmetric flow over ridges (Youngs et al., 2017), which can enhance the net momentum sink due to topographic form stress. Therefore, as an alternative to the common view that baroclinic instability is an integral component of eddy saturation, we propose that eddy saturation occurs as a consequence of feedbacks between transient eddies and the mean flow which creates topographic form stress and, in turn, balances the momentum input from wind stress (Figures 4c and 4d).

Acknowledgments
We acknowledge fruitful discussions with Louis-Phillipe Nadeau, Callum Shakespeare, Kial Stewart, and William Young. We appreciate the constructive review comments by Dave Munday and an anonymous reviewer. Furthermore, N. C. C. is indebted to Alistair Adcroft, Angus Gibson, Bob Hallberg, and Aidan Heerdegen for their help regarding using MOM6. Numerical simulations were conducted on the Australian National Computational Infrastructure at ANU, which is supported by the Commonwealth of Australia. MOM6 code is available online (https://github.com/NOAA-GFDL/MOM6). The model setup for the experiments presented can be found online (https://github.com/navidcy/EddySaturation-MOM6/). Model output is available online (https://doi.org/10.5281/zenodo.3246030). Scripts for producing figures are also available online (https://github.com/navidcy/EddySaturation-BtBc-GRL).

References

Abernathey, R., & Cessi, P. (2014). Topographic enhancement of eddy efficiency in baroclinic equilibration. *Journal of Physical Oceanography*, *44*(8), 2107–2126. https://doi.org/10.1175/JPO-D-14-0014.1

Adcroft, A., Anderson, W., Balaji, V., Blanton, C., Bushuk, M., Dufour, C. O., et al. (2019). The GFDL global ocean and sea ice model OM4.0: Model description and simulation features. *Journal of Advances in Modeling Earth Systems*, *11*. https://doi.org/10.1029/2019MS001726

Böning, C. W., Dispert, A., Visbeck, M., Rintoul, S. R., & Schwarzkopf, F. U. (2008). The response of the Antarctic Circumpolar Current to recent climate change. *Nature Geoscience*, *1*(1), 864–869. https://doi.org/10.1038/ngeo362

Barthel, A., Hogg, A. McC., Waterman, S., & Keating, S. (2017). Jet–topography interactions affect energy pathways to the deep Southern Ocean. *Journal of Physical Oceanography*, *47*(7), 1799–1816. https://doi.org/10.1175/JPO-D-16-0220.1

Bracegirdle, T. J., Shuckburgh, E., Sallee, J.-B., Wang, Z., Meijers, A. J. S., Bruneau, N., et al. (2013). Assessment of surface winds over the Atlantic, Indian, and Pacific Ocean sectors of the Southern Ocean in CMIP5 models: Historical bias, forcing response, and state dependence. *Journal of Geophysical Research: Atmospheres*, *118*, 547–562. https://doi.org/10.1002/jgrd.50153

Charney, J. G., & Flierl, G. R. (1980). Oceanic analogues of large-scale atmospheric motions. In B. A. Warren & C. Wunsch (Eds.), *Evolution of physical oceanography*. The MIT Press.

Chelton, D. B., deSzoeke, R. A., Schlax, M. G., Naggar, K. E., & Siwertz, N. (1998). Geographical variability of the first baroclinic Rossby radius of deformation. *Journal of Physical Oceanography*, *28*, 433–460.

Constantinou, N. C. (2018). A barotropic model of eddy saturation. *Journal of Physical Oceanography*, *48*(2), 397–411. https://doi.org/10.1175/JPO-D-17-0182.1

Constantinou, N. C., & Young, W. R. (2017). Beta-plane turbulence above monoscale topography. *Journal of Fluid Mechanics*, *827*, 415–447. https://doi.org/10.1017/jfm.2017.482

Cunningham, A. P., & Barker, P. F. (1996). Evidence for westward-flowing Weddell Sea deep water in the Falkland trough, western South Atlantic. *Deep-sea research I*, *43*(5), 643–654. https://doi.org/10.1016/0967-0637(96)00034-9

Donohue, K. A., Tracey, K. L., Watts, D. R., Chidichimo, M. P., & Chereskin, T. K. (2016). Mean Antarctic Circumpolar Current transport measured in Drake Passage. *Geophysical Research Letters*, *43*, 11,760–11,767. https://doi.org/10.1002/2016GL070319

Dufour, C. O., Le Sommer, J., Zika, J. D., Gehlen, M., Orr, J. C., Mathiot, P., & Barnier, B. (2012). Standing and transient eddies in the response of the Southern Ocean meridional overturning to the Southern Annular Mode. *Journal of Climate*, *25*, 6958–6974. https://doi.org/10.1175/JCLI-D-11-00309.1

Farneti, R., Delworth, T. L., Rosati, A. J., Griffies, S. M., & Zeng, F. (2010). The role of mesoscale eddies in the rectification of the Southern Ocean response to climate change. *Journal of Physical Oceanography*, *40*(7), 1539–1557. https://doi.org/10.1175/2010JPO4353.1

Farneti, R., Downes, S. M., Griffies, S. M., Marsland, S. J., Behrens, E., Bentsen, M., et al. (2015). An assessment of Antarctic Circumpolar Current and Southern Ocean meridional overturning circulation during 1958–2007 in a suite of interannual CORE-II simulations. *Ocean Modelling*, *93*, 84–120. https://doi.org/10.1016/j.ocemod.2015.07.009

Ferrari, R., Jansen, M. F., Adkins, J. F., Burke, A., Stewart, A. L., & Thompson, A. F. (2014). Antarctic sea ice control on ocean circulation in present and glacial climates. *Proceedings of the National Academy of Sciences of the United States of America*, *111*(24), 8753–8758. https://doi.org/10.1073/pnas.1323922111

Firing, Y. L., Chereskin, T. K., & Mazloff, M. R. (2011). Vertical structure and transport of the Antarctic Circumpolar Current in Drake Passage from direct velocity observations. *Journal of Geophysical Research*, *116*, C08015. https://doi.org/10.1029/2011JC006999

Hallberg, R., & Gnanadesikan, A. (2001). An exploration of the role of transient eddies in determining the transport of a zonally reentrant current. *Journal of Physical Oceanography*, *31*(11), 3312–3330. https://doi.org/10.1175/1520-0485(2001)031h3312:AEOTROi2.0.CO;2

Hallberg, R., & Gnanadesikan, A. (2006). The role of eddies in determining the structure and response of the wind-driven Southern Hemisphere overturning: Results from the modeling eddies in the Southern Ocean (MESO) project. *Journal of Physical Oceanography*, *36*, 2232–2252. https://doi.org/10.1175/JPO2980.1

Hart, J. E. (1979). Barotropic quasi-geostrophic flow over anisotropic mountains. *Journal of the Atmospheric Sciences*, *36*(9), 1736–1746. https://doi.org/10.1175/1520-0469(1979)036h1736:BQGFOAi2.0.CO;2

Hogg, A. McC., Meredith, M. P., Blundell, J. R., & Wilson, C. (2008). Eddy heat flux in the Southern Ocean: Response to variable wind forcing. *Journal of Climate*, *21*, 608–620. https://doi.org/10.1175/2007JCLI1925.1

Hogg, A. McC., Meredith, M. P., Chambers, D. P, Abrahamsen, E. P., Hughes, C. W., & Morrison, A. K. (2015). Recent trends in the Southern Ocean eddy field. *journal of Geophysical Research: Oceans*, *120*, 257–267. https://doi.org/10.1002/2014JC010470

Johnson, G. C., & Bryden, H. L. (1989). On the size of the Antarctic Circumpolar Current. *Deep-sea research*, *36*(1), 39–53. https://doi.org/10.1016/0198-0149(89)90017-4

Katsumata, K. (2017). Eddies observed by Argo floats. Part II: Form stress and streamline length in the Southern Ocean. *Journal of Physical Oceanography*, *47*, 2237–2250. https://doi.org/10.1175/JPO-D-17-0072.1

LaCasce, J. H. (2012). Surface quasigeostrophic solutions and baroclinic modes with exponential stratification. *Journal of Physical Oceanography*, *42*(4), 569–580. https://doi.org/10.1175/JPO-D-11-0111.1

Marshall, G. J. (2003). Trends in the Southern Annular Mode from observations and reanalyses. *Journal of Climate*, *16*, 4134–4143. https://doi.org/10.1175/1520-0442(2003)016h4134:TITSAMi2.0.CO;2

Marshall, D. P., Abhaum, M. H. P., Maddison, J. R., Munday, D. R., & Novak, L. (2017). Eddy saturation and frictional control of the Antarctic Circumpolar Current. *Geophysical research letters*, *44*, 286–292. https://doi.org/10.1002/2016GL071702

Masich, J., Chereskin, T. K., & Mazloff, M. R. (2015). Topographic form stress in the Southern Ocean State Estimate. *journal of Geophysical Research: Oceans*, *120*, 7919–7933. https://doi.org/10.1002/2015JC011143

Meredith, M. P., Naveira Garabato, A. C., Hogg, A. McC., & Farneti, R. (2012). Sensitivity of the overturning circulation in the Southern Ocean to decadal changes in wind forcing. *Journal of Climate*, *25*, 99–110. https://doi.org/10.1175/2011JCLI4204.1

Munday, D. R., Johnson, H. L., & Marshall, D. P. (2013). Eddy saturation of equilibrated circumpolar currents. *Journal of Physical Oceanography*, *43*, 507–532. https://doi.org/10.1175/JPO-D-12-095.1

Munk, W. H., & Palmén, E. (1951). Note on the dynamics of the Antarctic Circumpolar Current. *Tellus*, *3*, 53–55. https://doi.org/0.1111/j.2153-3490.1951.tb00776.x

Nadeau, L.-P., & Straub, D. N. (2012). Influence of wind stress, wind stress curl, and bottom friction on the transport of a model Antarctic Circumpolar Current. *Journal of Physical Oceanography*, *42*(1), 207–222. https://doi.org/10.1175/JPO-D-11-058.1

Olbers, D., Borowski, D., Voölker, C., & Wölff, J.-O. (2004). The dynamical balance, transport and circulation of the Antarctic Circumpolar Current. *Antiquités Science*, *4*, 439–470. https://doi.org/10.1017/S0954102004002251

Peña Molino, B., Rintoul, S. R., & Mazloff, M. R. (2014). Barotropic and baroclinic contributions to along-stream and across-stream transport in the Antarctic Circumpolar Current. *Journal of Geophysical Research: Oceans*, *119*, 8011–8028. https://doi.org/10.1002/2014JC010020

Rintoul, S. R., Sokolov, S., Williams, M. J. M., Peña Molino, B., Rosenberg, M., & Bindoff, N. L. (2014). Antarctic Circumpolar Current transport and barotropic transition at Macquarie ridge. *Geophysical Research Letters*, *41*, 7254–7261. https://doi.org/10.1002/2014GL061880

Risien, C. M., & Chelton, D. B. (2008). A global climatology of surface wind and wind stress fields from eight years of QuikSCAT scatterometer data. *Journal of Physical Oceanography*, *38*, 2379–2413. https://doi.org/10.1175/2008JPO3881.1

Stevens, D. P., & Ivchenko, V. O. (1997). The zonal momentum balance in an eddy resolving general circulation model of the Southern Ocean. *Quarterly Journal of the Royal Meteorological Society*, *123*(540), 929–951. https://doi.org/10.1002/qj.49712354008

Straub, D. N. (1993). On the transport and angular momentum balance of channel models of the Antarctic Circumpolar Current. *Journal of Physical Oceanography*, *23*, 776–782. https://doi.org/10.1175/1520-0485(1993)023h0776:OTTAAMi2.0.CO;2

Swart, N. C., & Fyfe, J. C. (2012). Observed and simulated changes in the Southern Hemisphere surface westerly wind-stress. *Geophysical Research Letters*, *39*, L16711. https://doi.org/10.1029/2012GL052810

Talley, L. D. (2013). Closure of the global overturning circulation through the Indian, Pacific, and Southern Oceans: Schematics and transports. *Oceanography*, *26*(1), 80–97. https://doi.org/10.5670/oceanog.2013.07

Tansley, C. E., & Marshall, D. P. (2001). On the dynamics of wind-driven circumpolar currents. *Journal of Physical Oceanography*, *31*, 3258–3273. https://doi.org/10.1175/1520-0485(2001)031h3258:OTDOWDi2.0.CO;2

Thompson, A. F., & Naveira Garabato, A. C. (2014). Equilibration of the Antarctic Circumpolar Current by standing meanders. *Journal of Physical Oceanography*, *44*(7), 1811–1828.

Toggweiler, J. R., Russell, J. L., & Carson, S. R. (2006). Midlatitude westerlies, atmospheric CO_2, and climate change during the ice ages. *Paleoceanography*, *21*, PA2005. https://doi.org/10.1029/2005PA001154

Treguier, A. M., & McWilliams, J. C. (1990). Topographic influences on wind-driven, stratified flow in a β-plane channel: An idealized model for the Antarctic Circumpolar Current. *Journal of Physical Oceanography*, *20*(3), 321–343. https://doi.org/10.1175/1520-0485(1990)020h0321:TIOWDSi2.0.CO;2

Ward, M. L., & Hogg, A. McC. (2011). Establishment of momentum balance by form stress in a wind-driven channel. *Ocean Modelling*, *40*(2), 133–146. https://doi.org/10.1016/j.ocemod.2011.08.004

Youngs, M. K., Thompson, A. F., Lazar, A., & Richards, K. J. (2017). ACC meanders, energy transfer, and mixed barotropic-baroclinic instability. *Journal of Physical Oceanography*, *47*, 1291–1305. https://doi.org/10.1175/JPO-D-16-0160.1